Geophysical Journal International

Geophys. J. Int. (2022) **0**, 1–0 https://doi.org/10.1093/gji/ggac170

GJI Geodynamics and Tectonics

Coseismic deformation and slip distribution of the 2017 M_w 6.3 Jinghe earthquake, Xinjiang, western China based on InSAR observations: a buried reverse event on previously unknown fault

Dong Yanfang, Meng Guojie and Hong Shunying

Institute of Earthquake Forecasting, China Earthquake Administration, Beijing 100036*, China, E-mail: guojiemeng@126.com; mgj@ief.ac.cn*

Accepted 2022 0. Received 2022 April 17; in original form 2021 June 1

SUMMARY

The 2017 M_w 6.3 Jinghe earthquake occurred in the orogenic zone of the North Tianshan mountain range, Xinjiang, western China. No evident surface rupture was identified by field investigation conducted immediately after the earthquake. We investigate the coseismic and post-seismic deformation fields due to the Jinghe event using the C-band Sentinel-1 SAR imagery, and further analyse its causative fault. The Generic Atmospheric Correction Online Service for InSAR (GACOS) model is employed to remove the atmospheric phase delay of multiple InSAR deformation maps. Coseismic deformation fields are resolved by averaging the high quality deformation maps. A nonlinear inversion scheme is used to find the optimized fault geometry in a layered elastic crust. The results imply that the Jinghe earthquake is characterized by thrust faulting, with striking and dipping angles of $\sim 62^\circ$ and $\sim 28^\circ$, respectively. Subsequently coseismic slip distribution is estimated using the steepest descent method program, constrained by the derived coseismic deformation fields. The inversion results show that the average slip is ~ 0.08 m and the average rake angle is $\sim 98^\circ$. The maximum slip is ~ 0.24 m, located at the depth of 12.9 km. The moment magnitude is estimated to be M_w 6.38. The fault geometry is generally consistent with the relocated aftershocks distribution. Both the InSAR-derived deformation field and the aftershock distribution indicate that the Jinghe earthquake is attributed to a previously unknown buried fault beneath the Yongji fold with a strike of 62°. No significant post-seismic deformation is identified in the zone of coseismic deformation. This study shows that the Jinghe earthquake is a typical inland thrust event in the North Tianshan area, which is affected by south to north compression due to the Indian-Eurasian collision.

Key words: Radar interferometry; Satellite geodesy; Dynamics: seismotectonics; Dynamics and mechanics of faulting.

1 INTRODUCTION

Coseismic deformation plays an important role in characterizing seismogenic fault and earthquake dynamics. Interferometric Synthetic Aperture Radar (InSAR) is an effective technique in deriving coseismic deformation. InSAR-derived coseismic deformation can be employed to invert for earthquake source parameters and slip distribution, beneficial to understanding the characteristics of tectonic stress in seismic zone. The SAR data, acquired by European Space Agency's (ESA) Sentinel-1 constellation, are widely used for studying crustal deformation due to earthquakes at continental scales, thanks to its large frame coverage and open sharing policy (Jiang *et al.* 2016; Sun *et al.* 2016; Wen *et al.* 2016). Several InSAR data processing approaches, such as Small Baseline Subsets (SBAS; Berardino *et al.* 2002) and Permanent Scatters (PS) methods (Ferretti *et al.* 2001), have been used to derive surface deformation at millimetre scale.

InSAR observations are mainly affected by topographic errors, orbital errors and atmospheric delays. Topographic phase can be removed using digital elevation model (DEM). Orbital errors can be reduced by precise orbit data. Atmospheric (including tropospheric and ionospheric) phase delays between the master and slave SAR images dominate the InSAR observation errors. For short-wavelength SAR data, ionospheric effects can be ignored because they are inversely proportional to the radar frequency (Meyer *et al.* 2006; Jung *et al.* 2013; Liu *et al.* 2014; Jung & Lee 2015; Feng *et al.* 2017; Lee *et al.* 2017). To measure the coseismic deformation of a large earthquake using InSAR, the tropospheric effect may be a relatively minor contribution. However, tropospheric effect is the main error source in the measurement of a smaller deformation (i.e. at centimetre to millimetre level), such as interseismic deformation, post-seismic deformation and coseismic deformation with a medium-small magnitude. It is difficult to derive smaller deformation only using traditional InSAR techniques. Stacking is an effective way to reduce the non-topography-related atmospheric noise. Lee *et al.* (2017) used a stacking method to minimize tropospheric errors to identify small coseismic deformation at the centimetre level. Fattahi *et al.* (2015) employed an ERA-Interim global atmospheric reanalysis model to correct the stratified tropospheric delay. Feng *et al.* (2016) adopted Medium Resolution Imaging Spectrometer (MERIS) near-IR water vapour data to correct RADARSAT-2 SAR data. However, the tropospheric models above have lower spatial and temporal resolutions, not suitable for the processing of Sentinel-1 data. Yu *et al.* (2017) developed the Generic Atmospheric Correction Online Service for InSAR (GACOS) model. The GACOS model was used to extract the small coseismic deformation of the 2017 M_w 6.4 Nyingchi earthquake and obtained improved interferograms compared to traditional phase analysis methods (Yu *et al.* 2018; Yu *et al.* 2020).

The 2017 M_w 6.3 Jinghe, Xinjiang earthquake occurred to the east of the known Kusongmuqike piedmont fault on 2017 August 8 by the United States Geological Survey (USGS). In the past decades, no earthquakes greater than M_w 4.0 happened in surrounding regions except an M_w 4.8 earthquake which occurred on 2011 October 16, 26 km to the west of the main shock, from the Global Centroid Moment Tensor (GCMT). Focal mechanism solution shows that the earthquake is a pure thrust event (Chen *et al.* 2012). The local stress distribution was studied from the nearby known fault parameters (i.e. strike and dip) and earthquake mechanisms, and found that Tianshan region is dominated by compressive stressing (Liu *et al.* 2019). The spatial distribution of relocated aftershocks suggested that the seismogenic fault plane was south-dipping (Liu *et al.* 2017). The geological setting and aftershocks imply that the Jinghe earthquake is associated with a new fault intersecting with the active thrust Kusongmuqike piedmont fault, which is in the North Tianshan orogenic zone with a relatively slow movement in its eastern part. The Kusongmuqike piedmont fault is about 160 km long, trending nearly east-west, and dipping towards south with an angle of 40–60° (Liu *et al.* 2017).

In order to understand the stress regime in the epicentral area, it is necessary to study the mechanism of the M_w 6.3 Jinghe earthquake. Liu *et al.* (2018) and Gong *et al.* (2019) inferred the focal mechanism of the 2017 Jinghe earthquake using Sentinel-1 SAR data. However, they did not consider the atmospheric delay in their InSAR processing. Liu *et al.* (2018) assumed the fault is north-dipping and claimed that the seismogenic fault is Kusongmuqike piedmont fault. Gong *et al.* (2019) employed multisensor observations to map the coseismic deformation, and modelled the slip distribution with different fault models according to published focal mechanism solutions, assuming that the fault strikes east-west (USGS solution) with southward and northward dipping, respectively. Their results showed that the seismic source is an east-west striking and south-dipping fault. Liu *et al.* (2018) and Gong *et al.* (2019) obtained different fault models. As such, it is needed to further refine the source model of the Jinghe earthquake. Meanwhile, the post-seismic deformation of the event has not been studied, thus the relationship between coseismic and post-seismic deformation fields is still unknown.

In this study, we derive the coseismic deformation field of the Jinghe earthquake by using multiple interferograms from ascending and descending orbits acquired by Sentinel-1A. Considering the centimetre scale deformation of the event, the GACOS model is used to eliminate the atmospheric delays for each interferogram. The averaged deformation fields are obtained from the improved interferograms. The fault geometry parameters, including fault length, width, buried depth, dip and strike, are derived based on the combination of ascending and descending line of sight (LOS) deformation. We invert for the slip distribution of the main shock, constrained by the InSAR deformation fields. Meanwhile, we analyse the spatial correlation between the coseismic slip and aftershocks distribution. Furthermore, there is not notable post-seismic surface deformation observed after the earthquake. We find that the seismogenic fault is a new blind thrust fault beneath the Yongji fold, which is consistent with the northern movement of the Indian plate. The clarification of the seismic fault model is helpful to studying regional tectonic background. This study is conducive to understanding the movement and seismic risk of the fold and thrust fault system in the North Tianshan area.

2 SEISMOTECTONIC SETTING

The Tianshan orogenic zone, located between the Jungar Basin and Tarim Basin, is characterized by strong seismic activity (Fig. 1). The uplift of the Tianshan mountain was formed by the Indian-Eurasian collision and the northward movement of the Pamir Plateau since the Cenozoic (Sun & Zhang 2009). Topographic map shows that thrust structure with a gentle dip angle dominate there. The earthquakes have deep focal sources and insignificant surface ruptures. GNSS derived crustal velocity fields show that the upper crust is undergoing shortening (Zubovich *et al.* 2010). As shown by Fig. 1, the active faults are mainly east-west striking and are characterized by dominate thrusting or right-lateral slip, inferred from the focal mechanisms. The 2017 M_w 6.3 Jinghe earthquake occurred in the North Tianshan region. An M_w 4.8 earthquake occurred in its epicentral area on 2011 October 16. To the west of the event, there are three $M_w \geq 6.0$ historical earthquakes. To the south, the Kusongmuqike piedmont fault is a right-lateral thrust fault, trending southeastwards, composed of several detached segments in the east part. According to the earthquake catalogue of the China Earthquake Networks Center (CENC), the epicentre (44.27°N, 82.89°E) of the Jinghe earthquake is located at the east segment of the Kusongmuqike piedmont fault, with a shallow depth of 11 km (Table 1).

3 DATA AND METHODS

3.1 SAR data

The Sentinel-1A SAR data used for deriving coseismic deformation in this study are acquired from ESA, with an observation period from 2017 August 8 to December 17 (Supporting Information Table S1). One descending frame and two adjacent ascending frames covers the epicentral area (Fig. 1a). Eleven ascending (track T85) scenes and ten descending (track T63) scenes are collected to extract the coseismic deformation (Supporting Information Table S1). The interferometric processing is implemented by the InSAR Scientific Computing Environment (ISCE), an open source and modular software incorporating modern programming schemes (Rosen *et al.* 2012).

3.2 Coseismic deformation extraction

Referring to the SBAS method, we select interferograms based on the criteria of temporal baseline between 20 and 60 days and

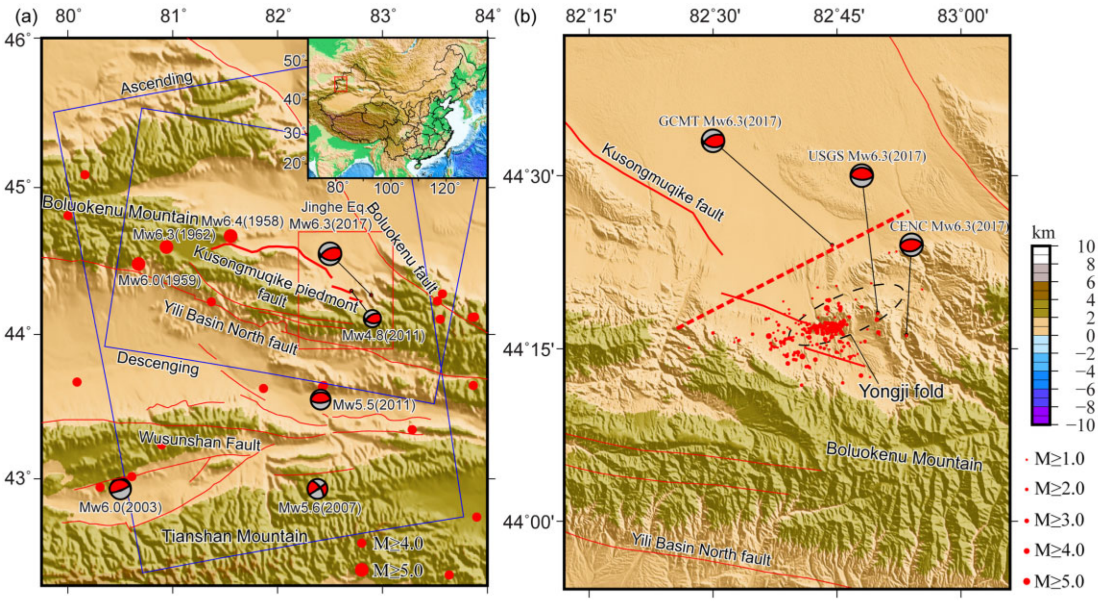

Figure 1. (a) Seismotectonic setting of the orogenic zone of the North Tianshan, Xinjiang, western China and SAR data coverage. The background is the 30 m shuttle radar topography mission (SRTM) digital elevation model (DEM). The two blue rectangles indicate the coverage of the Sentinel-1A SAR images acquired from ascending and descending orbits, respectively. The red solid lines represent the active fault traces from Seismic Active Fault Survey Data Center (SAFSDC). The beach balls represent the focal mechanism solutions ($>M_w$ 5.0 since the year 1958) from the U.S. Geological Survey (USGS) catalogue. The China Earthquake Networks Center (CNEC) M_w 6.3 event represents the main shock of the 2017 Jinghe earthquake sequence. Two red rectangles, with one in the upper right inset, represent the study area. Solid red circles represent historical earthquakes greater than M_w 5.0. (b) Close-up map of the 2017 Jinghe earthquake zone. Small solid red circles represent the relocated aftershocks (Liu *et al.* 2017). Beach balls represent the 2017 Jinghe main shock provided by various institutions—the Global Centroid Moment Tensor Project (GCMT), the USGS, and the CENC (Table 1). The red dashed line represents the seismogenic fault trace of the event projected on ground surface. The aftershocks relocated by the double-difference location approach during a 40-day period (Liu *et al.* 2017) were mainly distributed to the west of the main shock (Fig. 1b). The aftershocks are distributed over a depth range of 4–18 km. The source parameters of the Jinghe earthquake reported by the USGS, the CENC and the GCMT differ markedly from each other (Table 1).

Table 1. Focal mechanism solutions of the 2017 Jinghe main shock.

Source		Top fault centre X (°)	Y (°)	Depth (km)	Length (km)	Width (km)	Strike (°)	Dip (°)	Rake (°)	Strike slip (m)	Dip slip (m)	M_w
GBIS Result	Lower	−20 km	−30 km	15	10	4	50.0	20.0	–	−1	0	6.3
	Upper	20 km	−5 km	25	25	25	120.0	60.0	–	0.4	1.0	
	Optimal	11.2 km	−17.2 km	16.3	16.8	17.2	62.0	28.0	71	0.09	0.26	
	2.5%	10.7 km	−17.6 km	16.1	16.0	16.3	58.4	27.3	–	0.08	0.25	
	97.5%	11.7 km	−16.4 km	16.7	17.3	17.7	64.3	29.4	–	0.10	0.28	
	Uncertainties	−0.5/+0.5	−0.4/+0.8	−0.2/+0.4	−0.8/+0.5	−0.9/+0.5	−3.6/+2.3	−0.7/+1.4	–	−0.01/+0.01	−0.01/+0.02	
SDM Result		82.66	44.36	3.54			62	28	98	-	-	6.38
CENC		82.89	44.27	11.0	–	–	76	44	8099	–	–	6.3
							269	47				
USGS		82.83	44.30	20.0	–	–	92	60	92	–	–	6.3
							269	30	87			
GCMT		82.74	44.40	27.6	–	–	101	44	118	–	–	6.3
							244	52	66			

GBIS result is from Geodetic Bayesian Inversion Software, based on rectangular dislocation model with uniform slip. Depth denotes the depth of the lower edge. The *X and Y* are coordinates of the midpoint of the lower edge of the rectangular fault plane. Strike is measured clockwise from north. Dip angle is positive upward from horizontal. Strike slip is positive if right lateral and negative if left lateral. Dip slip is positive for thrust faulting and negative for normal faulting. Steepest descent method (SDM) result is derived from the slip distribution inversion based on the inferred coseismic deformation. The centre of the top edge of the fault plane is located at (44.36° N, 82.66° E) with a depth of 3.54 km. The source parameters were obtained from the China Earthquake Networks Center (CENC), the U.S. Geological Survey (USGS), and the Global Centroid Moment Tensor Project (GCMT), respectively.

perpendicular baseline < 60 m. The temporal and perpendicular baseline combination of Sentinel-1A data are shown in Fig. 2.

The precise orbit determination (POD) files and SRTM (Werner 2001) data with 1 arc-second (30 m × 30 m) spatial resolution are used to remove orbital and topographic contributions to the InSAR measurements, respectively. A phase filtering approach developed by Goldstein & Werner (1998) is employed to reduce phase noises. The Statistical-cost, Network-flow Algorithm for Phase Unwrapping (SNAPHU) program is adopted to unwrap the interferograms (Chen & Zebker 2001), and a threshold of 0.3 is used for phase unwrapping. Finally, the unwrapped phase maps are geocoded and converted into displacements in the LOS direction. The GACOS model is used to generate high-spatial resolution atmospheric delay maps. Tropospheric corrections are applied to the geocoded interferograms by subtracting the differential atmospheric delays,

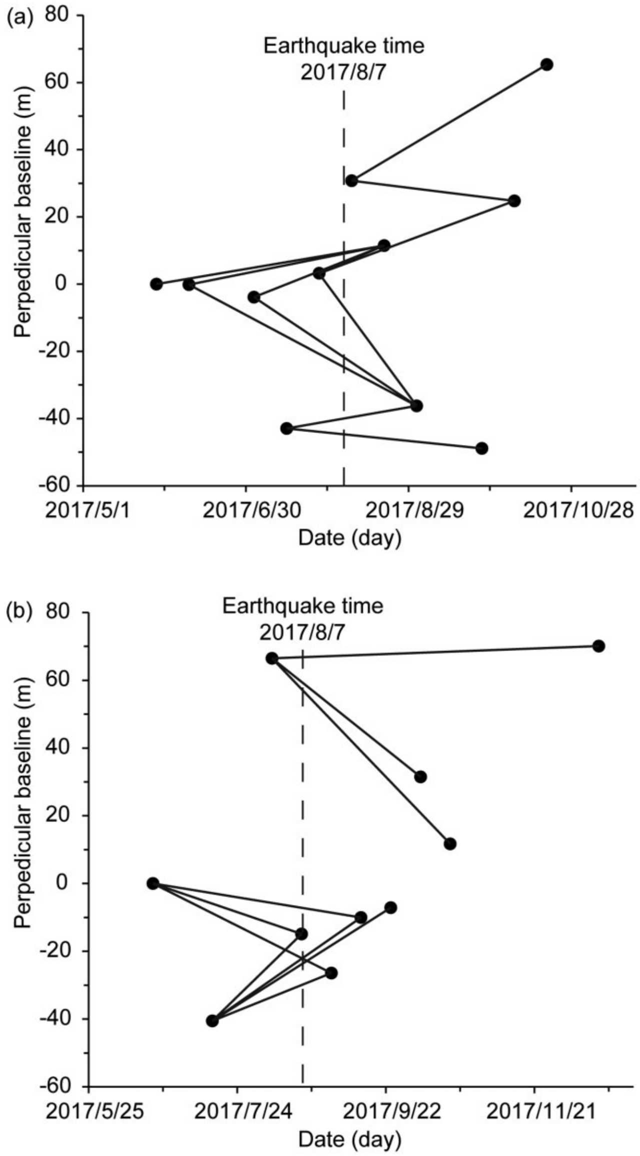

Figure 2. Temporal and perpendicular baselines of the interferogram pairs. (a) Ascending orbits. (b) Descending orbits. 12 ascending and 10 descending coseismic interferograms are selected.

and then multiple coseismic deformation maps are obtained for ascending and descending orbits, respectively. The improved interferograms with clearer coseismic signals are averaged to obtain the final coseismic deformation for ascending and descending orbits, respectively.

3.3 Slip inversion

We first use a uniform slip model to estimate the fault strike, width, dip, rake and location for a rectangular fault. Then, we use the source parameters to estimate the strike slip and dip slip with a variable slip model, assuming a homogeneous crust model and a layered crustal model, separately. Ascending and descending coseismic deformation data are utilized to invert for fault parameters by the Bayesian inversion approach via the GBIS, a MATLAB-based software package freely available to the scientific community (Bagnardi & Hooper 2018). Bayesian approach allows the inversion of multiple geodetic data-sets and rapid characterization of posterior probability density functions (PDFs) of source model parameters. Markov chain Monte Carlo (MCMC) method and Metropolis-Hasting algorithm are used to efficiently sample posterior PDFs with automatic step size selection. An optimal set of source parameters can be extracted from the posterior PDF by finding the maximum *a posteriori* probability solution. Finally, the fault model derived from Bayesian method and the down-sampled coseismic deformation data are employed to invert for slip distribution with the SDM through an iterative algorithm for the constrained least-squares optimization (Wang *et al.* 2013).

4 RESULTS

4.1 Deformation results

The GACOS tropospheric delay maps at 90 m resolution for every SAR data acquisition have been provided in a grid binary format (Yu *et al.* 2017). Our InSAR deformation or interferogram phase maps are obtained at 30 m resolution, and then they are down-sampled to 90 m resolution for the GACOS corrections. The GACOS zenith total delay maps of the corresponding interferogram pairs are shown in Figs 3 and 4. InSAR observations are relative to a reference point which is relatively stable in the deformation maps. We select the same reference point (44.44°N, 83.03°E) for all interferograms and zenith total delay maps in the multitemporal InSAR analysis (point P as shown in Fig. 5).

4.1.1 Ascending coseismic deformation

Fig. 3 shows the interferograms and coseismic deformation maps extracted from the twelve ascending image pairs in Fig. 2(a). The deformation map after correction shows a clearer coseismic deformation pattern and higher signal-to-noise ratio (Fig. 3). All of the interferograms have a pattern of ∼2 circles within the deformation area, corresponding to ∼5.6 cm deformation in the LOS direction. Most of the corrected coseismic deformation fields show an uplift displacement pattern. In Fig. 3(a), a localized uplift signal is present in the upper-left region, which is not found in other interferogram pairs after the atmospheric delay removal. This uplift signal in Fig. 3(a) possibly caused by the master image of 20170528, which is only used in this interferogram pair (Fig. 2a).

In Figs 3(b) and (c), the deformation patterns are not obvious with the common master image of 20170609. Fig. 3(d) has the same slave image (20170820) as Fig. 3(b), but shows a clear coseismic deformation pattern. This implies that the image of 20170703 has a better quality than 20170609. Generally, the signal-to-noise ratio of the coseismic deformation is improved after the atmospheric delay correction (Fig. 3). The standard phase deviation of the whole images is reduced averagely by 0.48 after the correction (Table 2), indicating that tropospheric vertical stratified phase delay exists in the interferogram phases. After the correction, the deformation maps from Figs 3(f), (h), (i) and (l) show clearer coseismic signals and less phase jumps than the original interferograms. And the four deformation fields are averaged to obtain the final ascending coseismic deformation map.

4.1.2 Descending coseismic deformation

Fig. 4 shows the interferograms and coseismic deformation maps extracted from the descending image pairs. The interferograms show

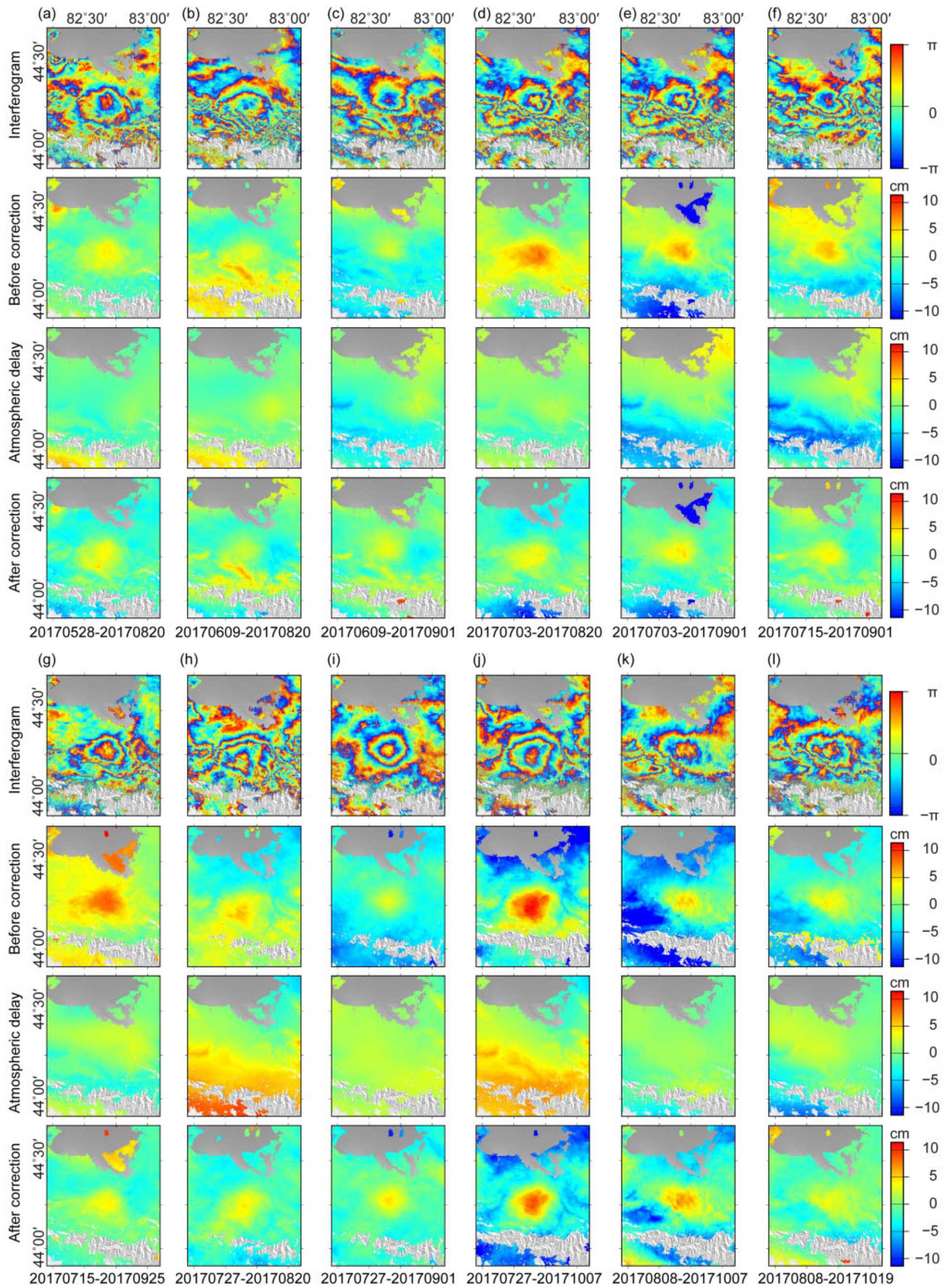

Figure 3. Coseismic interferograms and deformation maps derived from the Sentinel-1A SAR ascending orbits. From top to bottom for each pair are interferogram (where one fringe corresponds to 2.8 cm of displacement in the LOS direction), deformation before atmospheric delay removal, atmospheric delay and deformation after atmospheric delay removal. Each interferogram is named as master-slave date, for example 20170528–20170820. (a–l) 12 interferograms selected from the small baseline combination referred to Fig. 2(a), the master-slave dates of the 12 interferograms are, 20170528–20170820, 20170609–20170820, 20170609–20170901, 20170703–20170820, 20170703–20170901, 20170715–20170901, 20170715–20170925, 20170727–20170820, 20170727–20170901, 20170727–20171007, 20170808–20171007 and 20170808–20171019, respectively.

two circles (∼5.6 cm deformation in the LOS direction) in the deformation area. After applying the correction, the deformation maps of Figs 4(a), (d), (h) and (i) show better coseismic patterns and are averaged to obtain coseismic interferograms for the descending orbit.

4.2 Coseismic deformation extraction and seismogenic fault parameters inversion

4.2.1 Coseismic deformation extraction

After the atmospheric delay correction, we select the common reference point (P in Fig. 5) to normalize the multiple deformation maps. An equal weighting average method is used to derive the coseismic deformation for the ascending (Fig. 5a) and descending

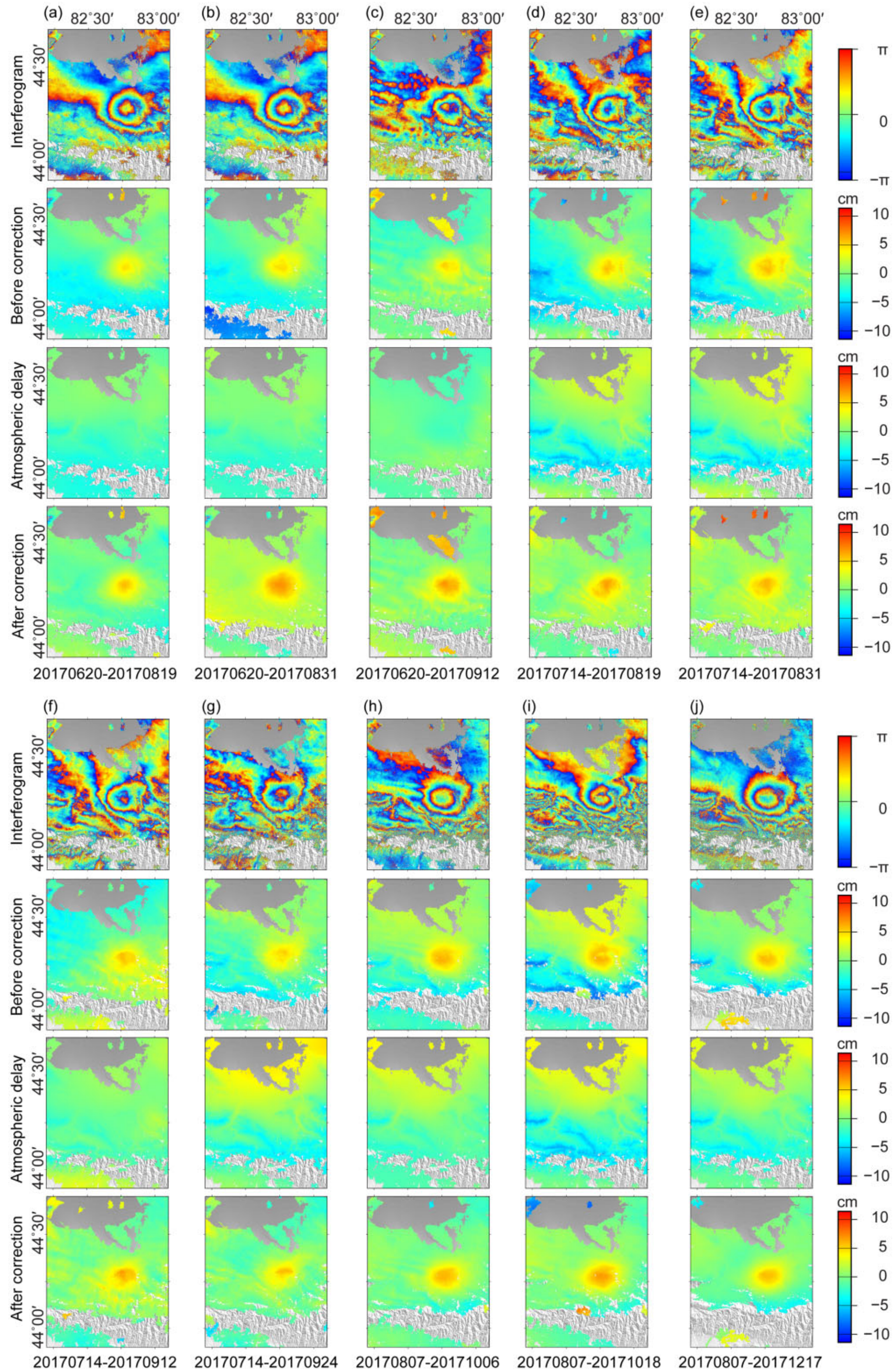

Figure 4. Same as Fig. 3, but for the descending orbits. (a–j) 10 interferograms selected from the small baseline combination referred to Fig. 2(b), the master-slave dates of the 10 interferograms are 20170620–20170819, 20170620–20170831, 20170620–20170912, 20170714–20170819, 20170714–20170831, 20170714–20170912, 20170714–20170924, 20170807–20171006, 20170807–20171018 and 20170807–20171217, respectively.

(Fig. 5b) orbits, respectively. For the ascending orbit, especially in Figs 3(d), (e), (j) and (k), short wavelength error is not reduced after the GACOS correction, which is not used in the weighting average. The average coseismic deformation is about 5–6 cm in the LOS direction. Some different displacements exist in Figs 5(a) and (b), due to the variable LOS direction for the ascending and descending orbit

Figs 5(c)–(f) show deformation maps derived by the stacking method directly using the pre-corrected interferograms. For the ascending orbit, phase jumps are not removed in the upper-left region

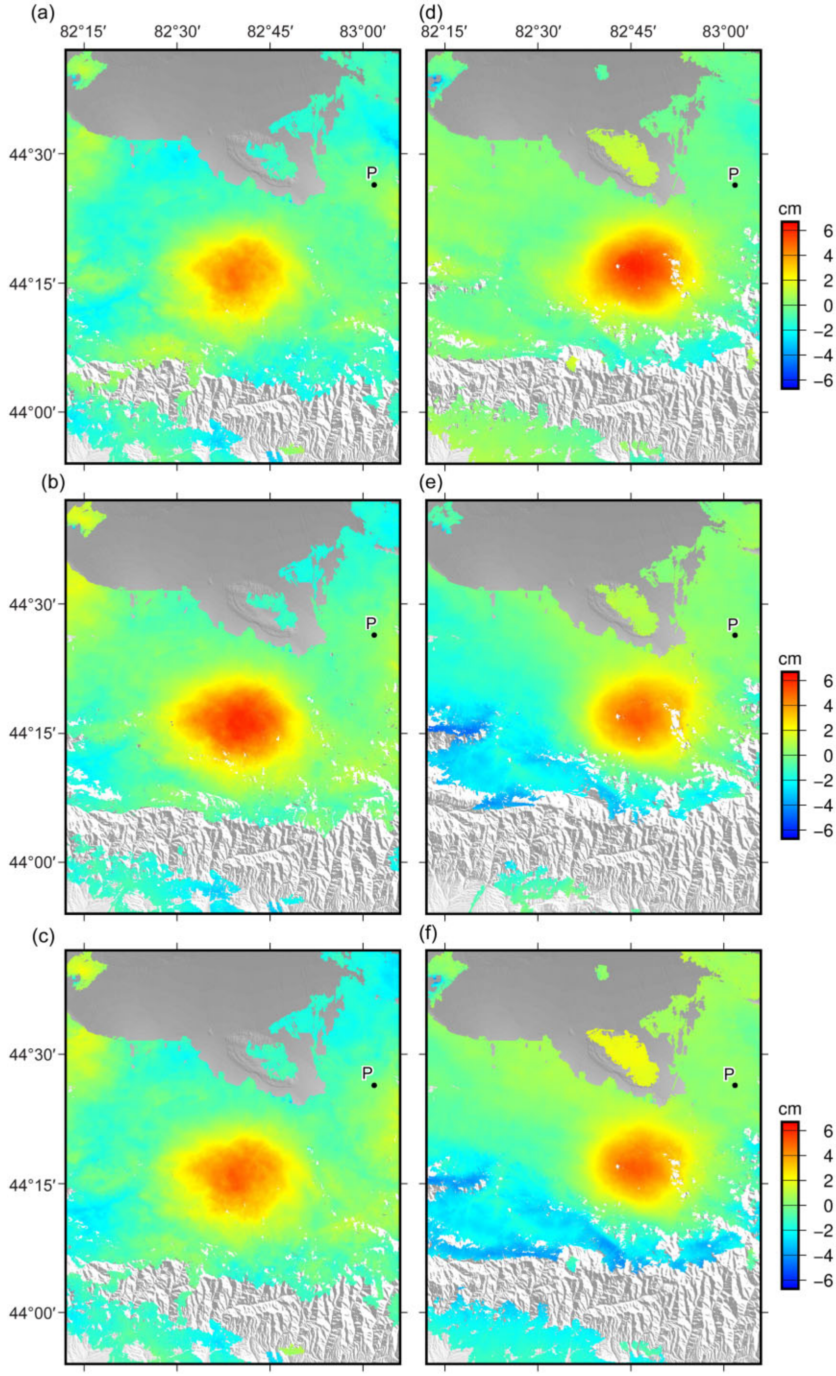

Figure 5. Coseismic deformation maps derived from Sentinel-1A InSAR observations. Point P is the reference point. Panels (a–c) show the average deformation of four interferograms (Figs 3f, h, i and l) after GACOS correction, stacking deformation of the 12 interferograms, and stacking deformation of the 4 interferograms without GACOS correction for the ascending orbit, respectively. (d–f) are the average deformation of 4 interferograms (Figs 4a, d, h and i) after GACOS correction, stacking deformation of the 10 interferograms, and stacking deformation of the 4 interferograms without GACOS correction for the descending orbit, respectively.

in Figs 5(b) and (c) for the ascending orbit, and atmospheric effect is not removed in Figs 5(e) and (f) for the descending orbit. By analysis, that the averaged InSAR deformation with the interferograms from GACOS correction has the minimum phase standard deviation (Table 3), and will be used in the inversion of fault geometry and slip distribution.

4.2.2 Inversion for seismogenic fault parameters

In order to study the causative mechanism of the Jinghe earthquake, we estimate the seismogenic fault parameters of the event using the GBIS (Bagnardi & Hooper 2018), under the assumption of a uniform slip. Adaptive quad-tree method is used to down-sample the ascending and descending deformation data. Constrained by the down-sampled data, we invert for parameters of a rectangular

Table 2. Phase standard deviations of the whole images before and after GACOS correction.

No.	Ascending orbit (T85) Interferogram pair	Before correction	After correction	Descending orbit (T63) Interferogram pair	Before correction	After correction
1	20170528–20170820	1.5062	1.9148∗	20170620–20170819	1.9741	1.3707
2	20170609–20170820	2.2139	2.0105	20170620–20170831	2.6552	1.4462
3	20170609–20170901	2.1623	1.6059	20170620–20170912	1.5519	1.6144∗
4	20170703–20170820	2.1480	2.4022∗	20170714–20170819	2.2316	1.4157
5	20170703–20170901	4.3175	3.6687	20170714–20170831	2.4769	1.3228
6	20170715–20170901	2.8692	1.5716	20170714–20170912	2.1549	1.5855
7	20170715–20170925	2.0639	1.8253	20170714–20170924	1.9109	1.4422
8	20170727–20170820	2.6698	1.7293	20170807–20171006	2.0637	1.4737
9	20170727–20170901	1.9909	1.6306	20170807–20171018	3.0236	1.8647
10	20170808–20171007	2.6698	1.7293	20170807–20171217	2.0816	1.5352
11	20170808–20171007	1.9076	1.3488			
12	20170808–20171019	2.4854	1.7795			

∗ Denotes the interferogram pairs whose standard phase deviations are not reduced after GACOS correction.

Table 3. Phase standard deviations of GACOS correction methods and stacking method.

	Ascending orbit (T85)	Stacking (cm)	GACOS (cm)	Descending orbit (T63)	Stacking (cm)	GACOS (cm)
1	12 interferograms	1.5976	1.8543	10 interferograms	1.7000	1.3569
2	Figs 3(f), (h), (i) and (l)	1.4353	1.3084	Figs 4(a), (d), (h) and (i)	1.7192	1.3084

dislocation source model of uniform slip (Okada 1985). In the GBIS inversion, the numerical ranges of fault geometry parameters are prescribed (Bagnardi & Hooper 2018).

Fig. 6 shows posterior PDFs for the nine fault source parameters obtained after 10^6 iterations (a burn-in period of 2×10^4 iterations is removed). The mean fault parameters are estimated by the Gaussian distribution statistics. The lowest sub-graphs show histograms of marginal distributions for each parameter and the remaining sub-graphs show the joint distributions between pairs of parameters. Lower and upper bounds of model parameters for the seismic source, optimal inversion results and the 95 per cent confidence intervals are shown in Table 1. Uncertainties of fault parameter are calculated from the optimal solution, 2.5 per cent and 95 per cent of posterior probability density functions (Table 1). From the marginal posterior probabilities in Fig. 6, we can also identify the correlations between the different fault parameters. Generally, the fault geometry parameters are well constrained. The rake angle (∼71°) is consistent with a dominant thrust fault, computed from the strike slip of 0.09 m and dip slip of 0.26 m. The inversion reveals that the seismogenic fault of the main shock is a thrust rupture with a south-dipping angle of ∼28° and a strike azimuth of ∼62°. The deformation residuals between the observation and prediction are generally less than 2 cm (Figs 7c and f).

We also invert for the fault geometry with a rectangular fault by the GBIS program, using a north-dipping model; however, we cannot derive a reasonable solution. The posterior PDFs of the north-dipping model parameter are shown in Supporting Information Fig. S1. We test different model parameters in order to obtain the optimal fault geometry. In the inversion, we adjust the upper bounds of the dip slip from 0.3 to 1.0 m. The estimated dip angle is ∼48° to 54°, and the strike is ∼258°. However, the inversed dip slip always falls on the upper bounds (Supporting Information Fig. S1), suggesting that we cannot get a reasonable dip slip using north-dipping model. In this study, we prefer the south-dipping model.

4.3 Coseismic slip model

4.3.1 Coseismic slip distribution inversion

With the optimized fault geometry (strike and dip), fault slip distributions are then inverted, constrained by the InSAR data. We employ the SDM (Wang *et al.* 2013) to perform the slip distribution inversion using a variable slip model. In order to cover the entire slip domain, the fault plane is extended as a rectangle with a length of 42 km and a width of 40 km, and divided into a set of small patches, each with a patch size of 3 km × 3 km. The Green's functions are calculated using a multilayered elastic half-space model (Wang *et al.* 2013). And the layered crust model from CRUST1.0 (Laske *et al.* 2013; Supporting Information Table S2) is used.

The rake angle is assumed to be 80–100° considering a pure thrust event from the source parameters reported by previous studies (Table 1). The depth of the top edge of the fault plane is set to 3.54 km, which meaning a buried fault according to the previous studies (Liu *et al.* 2017; Liu *et al.* 2018; Gong *et al.* 2019). During the inversion, the model parameters are optimized through repeated trial-and-error calculations (Wang *et al.* 2013). An identical weight is used for down-sampled data of ascending and descending orbits. We test various smoothing factors in the inversion procedure. The trade-off curve shows the relation between roughness and model-data misfit (Fig. 8), and the optimal smooth factor is set to 0.16.

The observed coseismic deformation, modelled deformation and their residuals for the ascending and descending orbits are shown in Fig. 9. The root mean square (RMS) error is about 0.4 cm (Fig. 9c) and 0.6 cm (Fig. 9c) for the ascending orbit and descending orbit, respectively. The modelling results show that the best data-model fit is achieved with a correlation coefficient of 0.98. The optimum results show that the Jinghe earthquake is characterized by a thrust motion with a rake angle of ∼98°.

The fault slip is mainly distributed between the depths of 8 and 17 km. The average slip value is ∼0.09 m and the maximum value is ∼0.24 m located at (44.21°E, 82.74°N), with a depth of ∼12.9 km.

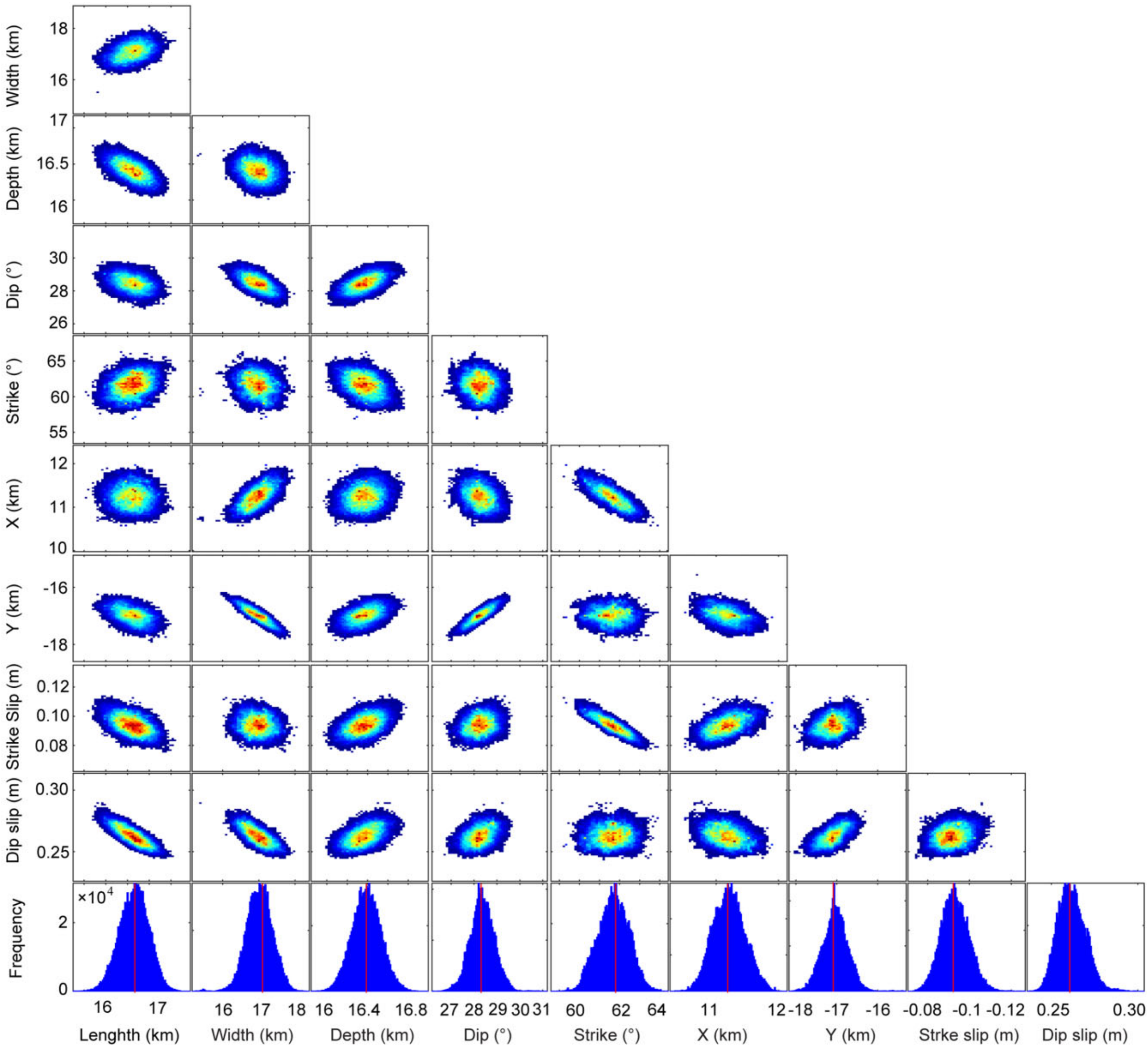

Figure 6. Marginal posterior probability distributions for the fault model parameters. Red lines present the maximum *a posteriori* probability solution. Scatter plots are contoured according to frequency.

Assuming a shear modulus of 30 GPa (Sieh 1978), the seismic moment calculated from the geodetically constrained finite slip model is 4.28 × 1018 Nm, equivalent to an event of M_w 6.38. Our result roughly agrees with the moment tensor solutions reported by the USGS, the CENC, and the GCMT (Table 1), in terms of the locations, strike, dip and rake.

In order to analyse the spatial correlation between the aftershocks and the slip distribution, we collect the $M > 1.0$ aftershocks over the 40-day period after the main shock. The relocated aftershocks are located to the west of the main shock (Figs 10a and b). The aftershocks mainly occurred at a depth less than 15 km and were concentrated at the nearby zone to the slip centre (Fig. 10d). We project the aftershocks to a plane perpendicular to the fault surface (Fig. 10d), showing the aftershocks distribution is generally consistent with the fault location.

In addition, we also resolve the coseismic slip distribution with a homogeneous crust model and compare it with the layered crust model (Supporting Information Fig. S2). There are no visible discrepancies on the slip distribution derived by the different crust model for this case.

4.3.2 The uncertainty of the slip distributions

The uncertainty of the slip distributions can be estimated by the integration of SDM and Monte Carlo (MC) method (Feng & Li 2010). 100 groups of InSAR measurement data with random noise are generated for the ascending and descending orbits using the MC method, respectively. The noises are synthetically produced through the full variance-covariance matrix (VCM) of the signals in the far-field. Using these InSAR data sets, we perform 100 inversions for fault slip distributions by the SDM method (Wang *et al.* 2013). The results are analysed statistically to calculate the standard deviation (uncertainty) of slip distributions (Fig. 11). The maximum

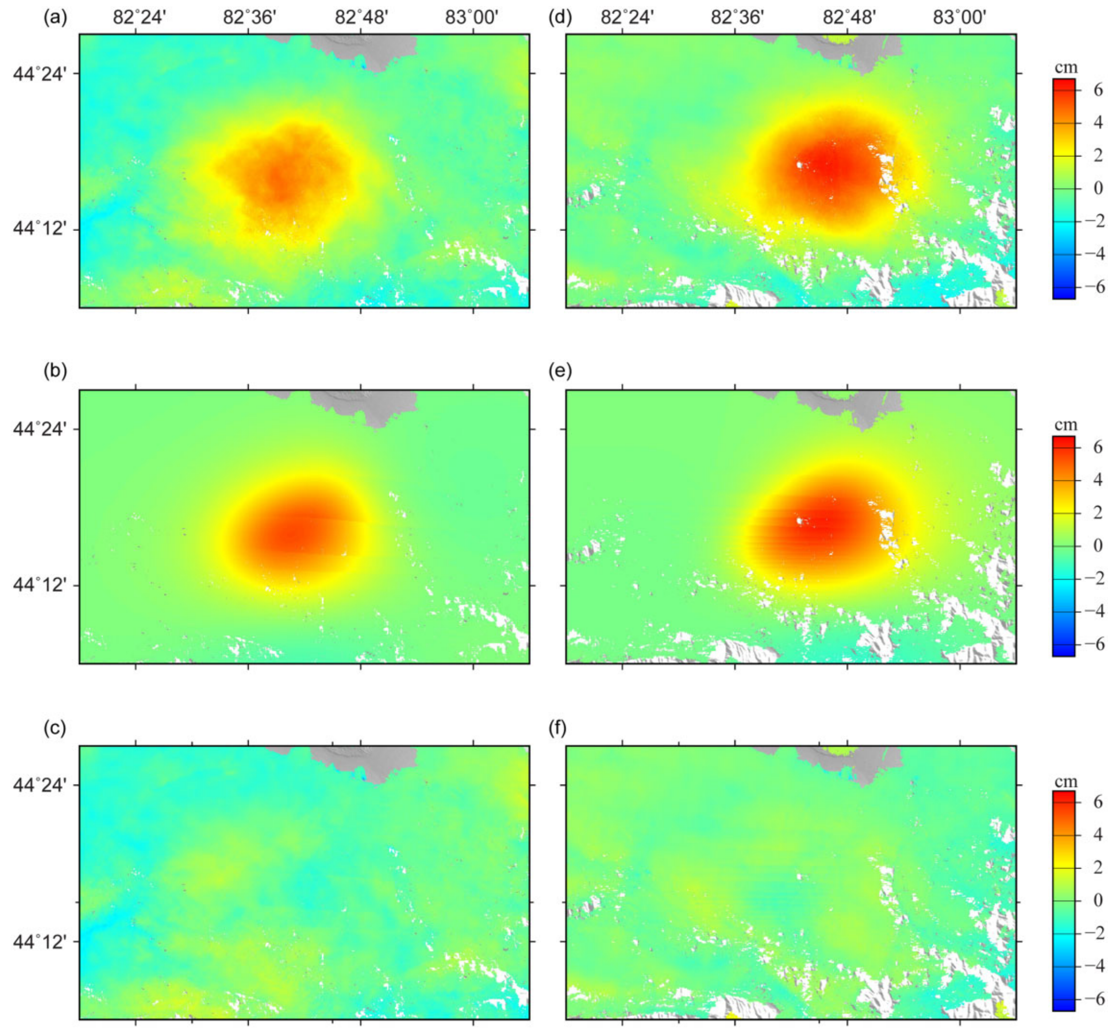

Figure 7. Simulations and residuals based on the optimal fault parameters. (a–c) Observed, simulation, and residual for ascending orbit deformation, respectively; (d–f) similar to (a)–(c), but for the descending orbit deformation.

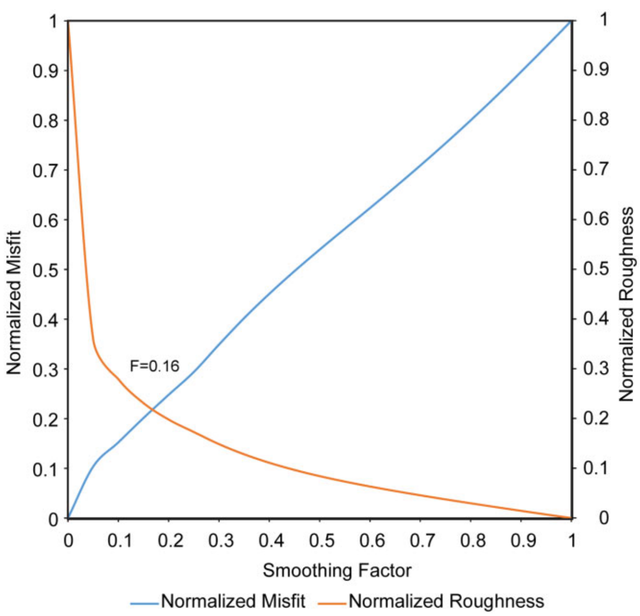

Figure 8. Trade-off curve between misfit and slip roughness. The preferred smoothing factor is 0.16.

uncertainty of the fault slip is about 2.1 cm below the slip centre (Fig. 11b), about 9 per cent of the maximum slip (0.24 m).

Supporting Information Fig. S3 shows the checkerboard test for the inversion of coseismic slip distribution. Most of the slip patches with a depth (along dip direction) smaller than 25 km are recovered in the checkerboard test. Therefore, the slip distribution has good resolution at the slip patches with depth smaller than 25 km, but the slip pattern is smeared at a larger depth. The checkerboard test shows that the inversion of InSAR data can provide a reasonable slip model for the Jinghe event.

5 DISCUSSION

5.1 Extracting coseismic deformation of moderate earthquake

Large shallow earthquakes might cause great deformation of tens of centimetres. Given the large signal-to-noise ratio, observation errors, such as atmospheric delays, are minor issues in the analysis of surface deformation. However, the surface deformation due to moderate and small magnitude earthquakes is relatively smaller, usually at the level of centimetres. Previous studies have indicated

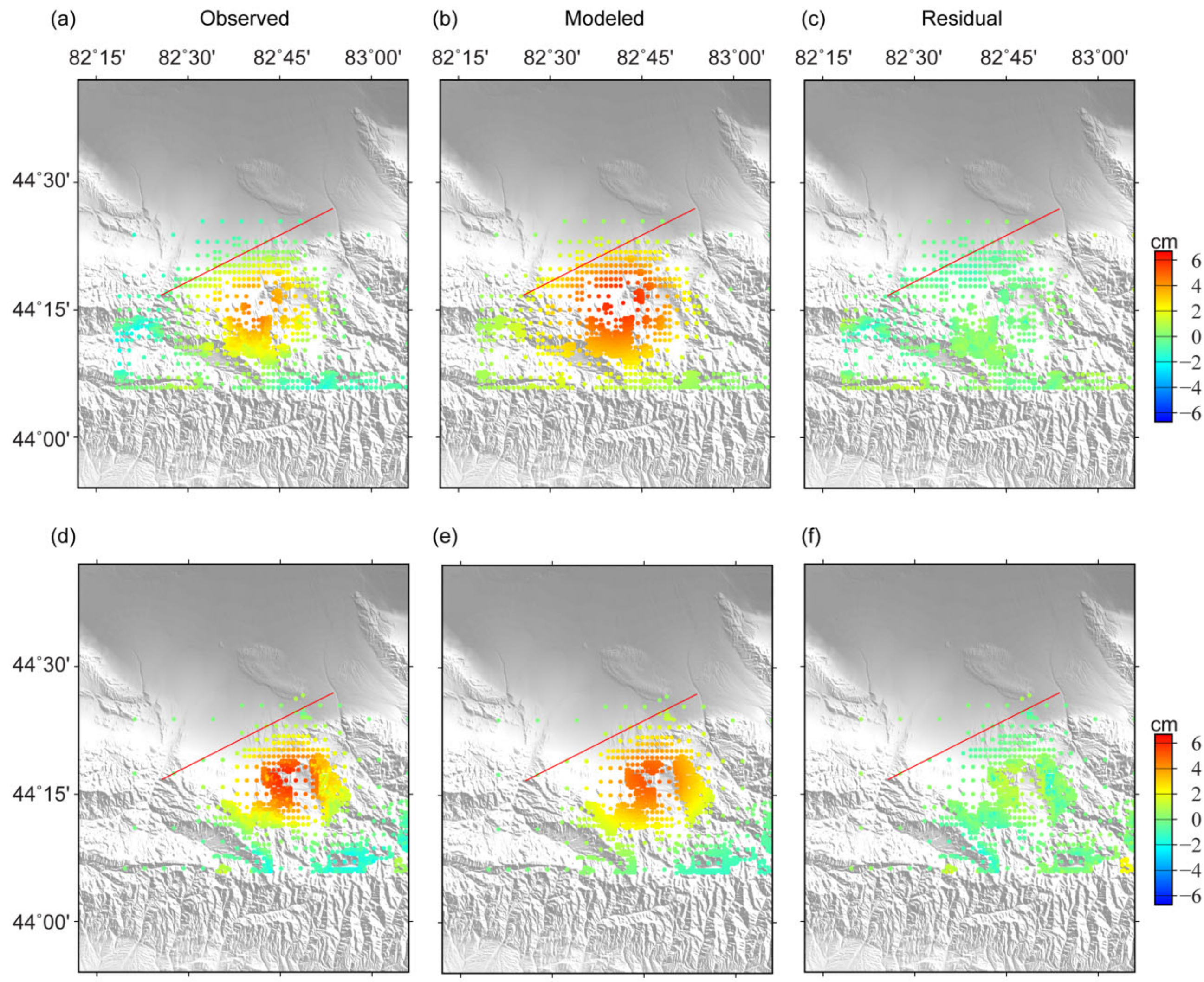

Figure 9. InSAR-derived deformation, modelled deformations and residuals. (a–c) Observed, modelled and residuals deformation for the ascending orbit data; (d–f) similar to (a)–(c), but for the descending orbit data.

that atmospheric artefacts may lead to errors of greater than 10 cm in surface deformation observations (Zebker *et al.* 1997; Lu & Dzurisin 2014). If the atmospheric phases in the interferometric processing are not properly corrected, it will be difficult to derive precisely small deformation through the InSAR observations.

External data, such as GNSS and meteorological data (Li 2005), Moderate Resolution Imaging Spectroradiometer (MODIS) observations (Li *et al.* 2005; Ding *et al.* 2008) and Medium Resolution Imaging Spectrometer (MERIS) data (Feng *et al.* 2016), could be used to correct atmospheric effects. Nonetheless, these approaches are not easily implemented due to the differences of spatial resolution and acquisition times between the external data and the acquired SAR images. Other methods, such as PS (Ferretti *et al.* 2001) and SBAS (Berardino *et al.* 2002), have been widely applied to atmospheric delay reduction. However, it is difficult to measure abrupt deformation from coseismic events, because a linear deformation model is assumed. In this study, multiple interferogram pairs are obtained based on temporal and spatial baseline thresholds. After the mitigation of orbital and topographic errors, the main error source left is atmospheric delay. Some interferogram pairs do not show clear coseismic deformation patterns because of the atmospheric delay effects (see the first row of each interferogram pair in Fig. 3). In order to extract the centimeter-level coseismic deformation of the Jinghe event, it is necessary to remove atmospheric delays more accurately.

As shown in Fig. 3, we can see that the atmospheric delay obtained from the GACOS model is dependent on the topography. Fig. 3 reveals that the data acquired on 20170901 and 20170727 were subject to more atmospheric delay, and the delays were well estimated and removed through the GACOS model (see the corrected coseismic deformation of 20170727–20170901 in Fig. 3i). For the descending orbit observations, multiple coseismic deformation maps (Fig. 4) reveal that the SAR data of 20170714 and 20170807 involved more atmospheric delays. Finally, the coseismic deformation is obtained by averaging the relatively good quality deformation maps obtained from the ascending and descending orbits, respectively (Fig. 5).

In addition, stacking method is also used to correct the atmospheric delay in this study. However, phase jump and atmospheric effects are not mitigated effectively via this approach. In the case of the Jinghe event, GACOS method generally gives better results than the stacking method. However, sometimes the GACOS model is not efficient (see Table 2). This means that when the atmospheric delay estimation is not accurate, the corrected results are not better, or even worse than those without correction.

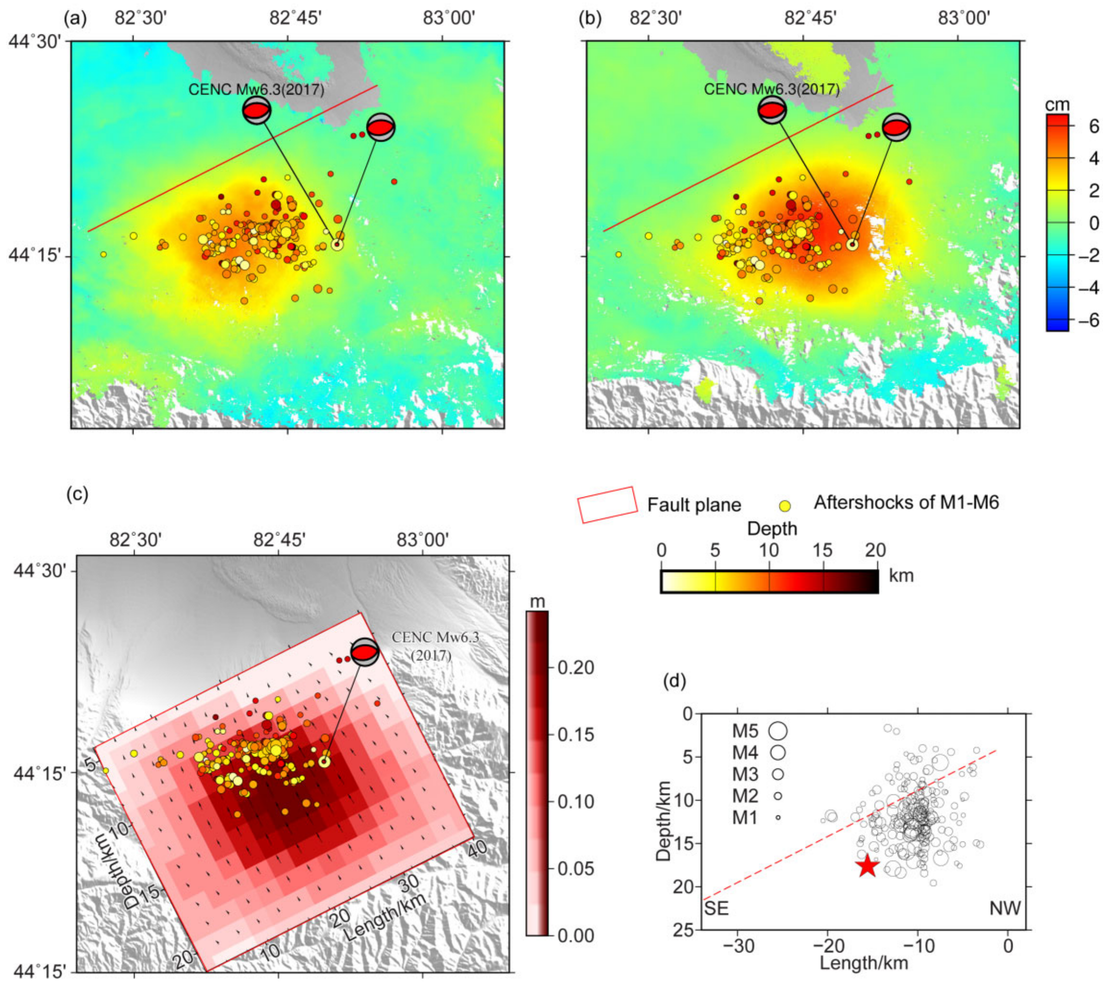

Figure 10. Fault slip and relocated aftershocks distribution. (a and b) Aftershocks superimposed on ascending and descending deformation maps, respectively. (c) Map view of the slip distribution projected to surface. The length of the fault plane is 42 km, the downdip depth is ∼22 km, and the dip angle is ∼28° to the southeast. The arrows represent the magnitude and azimuth of slips in fault patches. The solid circles indicate the relocated aftershocks. (d) Aftershocks distribution in vertical plane perpendicular to the fault plane.

The epicentral region of the Jinghe earthquake is sparsely populated, lacking in GNSS and seismic observation stations. InSAR technology therefore can be exploited to observe the coseismic deformation all day and under all weather conditions to study the causative mechanism of the event. Although Liu *et al.* (2018) and Gong *et al.* (2019) studied the focal mechanism of the 2017 Jinghe earthquake using Sentinel-1 SAR data, they did not consider the atmospheric delay in their InSAR coseismic deformation maps. According to our data processing in this study, the atmospheric delay should be considered in order to extract centimeter-level coseismic deformation. We use atmospheric correction and multitemporal analysis to improve the quality of the coseismic deformation maps. Our results show that the signal-to-noise ratio of coseismic deformation field is improved after the atmospheric correction (Table 2).

5.2 Characteristics of the focal mechanism and seismogenic fault

The 2017 Jinghe earthquake occurred in the north Tianshan region, with folds and thrust faults dominating there. Because of the collision between the Indian and Eurasian plates, the Tianshan region has experienced thrust from the south to the north in the western segment of the North Tianshan since the Cenozoic (Liu *et al.* 2019). Through the investigation of palaeoseismic deformation zone, Quaternary fault activity and river step dislocation, Chen *et al.* (2007) found that the Kusongmuqike piedmont fault is an active fault, showing more obvious thrust activity in the east section. The tectonic stress field implies a compression regime in the nearby region, and the surrounding faults are mainly NWW–SEE trending (Liu *et al.* 2019). This suggests that the 2017 Jinghe earthquake might be characterized by thrust faulting.

We use nonlinear Bayesian method (Bagnardi & Hooper 2018) to invert for the seismogenic fault parameters constrained by coseismic InSAR deformation field. The focal mechanisms reported by several organizations (Table 1) have moment magnitudes of M_w 6.2–6.4. The strike, rake and dip are similar, but the depths are different. All of these results show that the fault is nearly east-west trending with thrust movement, consistent with the sense of geological stress field. Our results inverted from the coseismic InSAR deformation reveal that the seismogenic fault has a strike of ∼62° and a mean rake angle of ∼98°, similar to the mechanism reported by the CENC. The maximum slip is ∼0.24 m, corresponding to a moderate earthquake. However, our dip angle is ∼28°, smaller than that provided by the CENC, USGS and GCMT.

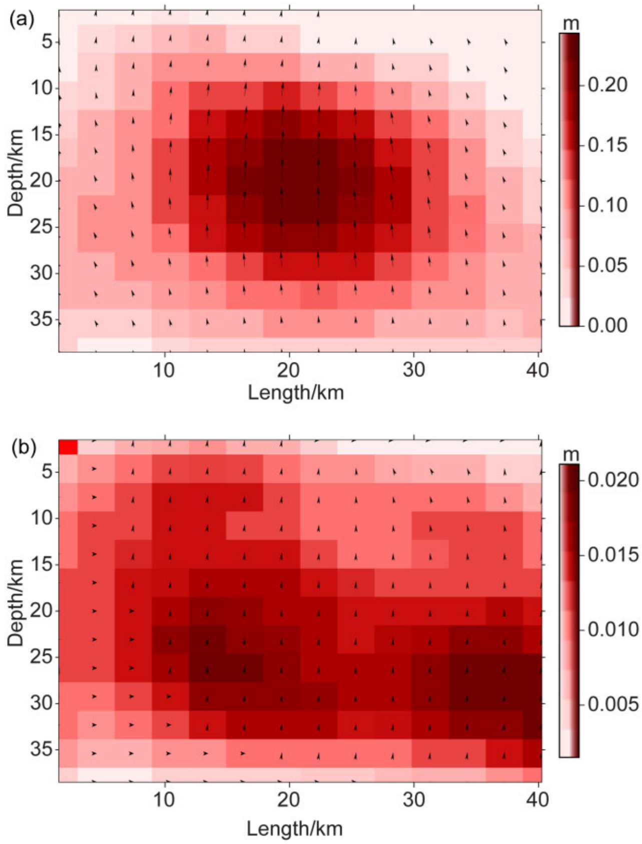

Figure 11. Coseismic slip distribution and its uncertainties in a 2-D projection. (a) Coseismic slip distribution. (b) Corresponding uncertainties of the fault slips. Black arrows indicate the magnitude and azimuth of slips in fault patches. The maximum slip uncertainty is ∼2.1 cm.

Liu *et al.* (2017) relocated the aftershock sequence based on the waveforms recorded by the Xinjiang Digital Seismic Network using the Double Difference relocation method. The aftershock sequence (Liu *et al.* 2017) and the back projection of the teleseismic recording (Zhang *et al.* 2020) demonstrated a unilateral rupture about 15–20 km to the west of the main shock. The aftershocks were nearly distributed in the SWW–NEE direction, which generally agreed with the results of Xu *et al.* (2019). The seismic sources of the aftershocks became deeper from north to south, indicating that the fault plane dips towards the south (Liu *et al.* 2017). Li & Wang (2019) used the cut and paste (CAP) method to invert for the focal mechanism parameters of $M > 3.0$ aftershocks. The focal mechanisms of most aftershocks were thrust, similar to that of the main shock. The focal source parameters indicated that the Jinghe earthquake sequence was dominated by a south to north compression stress field (Li & Wang 2019).

Liu *et al.* (2018) drew a conclusion that the seismogenic fault was the known Kusongmuqike piedmont fault, located to the south of the aftershock sequence and dipping towards north. Gong *et al.* (2019) found the optimal solution by trying various fault models dipping south and north separately. They tested fault models with strikes of 90°, 100°, 110° and 270°, located to the south and north of deformation field, respectively. They claimed the south-dipping and east-west striking model because it was more consistent with the aftershock sequence. In this study, we obtain more accurate deformation fields and invert for fault geometry with acceptable accuracy. Our results show that the seismogenic fault dips to the south with purely thrust characteristic, indicating that the earthquake activity is due to the stress from the collision between the Indian and Eurasian plates. Furthermore, our results imply that the seismogenic fault of the Jinghe event is not attributed to the known Kusongmuqike piedmont fault, but a blind thrust fault striking ∼62°, intersecting with the east section of the Kusongmuqike piedmont fault. According to the inversion results of focal parameters and the local geomorphic features, it is inferred that the seismogenic fault is a blind fault developed beneath the Yongji fold (Fig. 1b). This interpretation is consistent with the tectonic activities in the North Tianshan region: it is affected by south to north compression in alignment with the push direction of the Indian plate. This shows that the Jinghe earthquake is a typical inland thrust earthquake in the North Tianshan area. This study suggests that, in addition to large-scale active fault zones, the complex folds and thrust faults in the area may also lead to the risk of moderate or large earthquakes in the future.

5.3 Post-seismic deformation

We use the ascending and descending differential interferograms based on StaMPS method (Hooper *et al.* 2012) to derive post-seismic deformation spanning 2017 August 8 to 2020 June 17. The multitemporal Sentinel-1A SAR images, including 53 ascending and 44 descending images, are listed in Supporting Information Table S3. Time-series phase for each interferogram pair is smoothed using a Gaussian-weighted piecewise linear fitting. The spatially uncorrelated look angle error is estimated and subtracted from the wrapped phase of the selected PSs. PS phase is filtered using the Goldstein adaptive phase filter, and then unwrapped using the 3D phase unwrapping method (Hooper & Zebker 2007). Finally, the spatially correlated look angle error (DEM error), master atmosphere and orbit error are calculated and removed from the unwrapping phases. We use logarithmic (LOG) function to model the post-seismic deformation. Then, the deformation time-series referenced to the first SAR scene is obtained (Supporting Information Fig. S4 for ascending orbit T85 and Supporting Information Fig. S5 for descending orbit T63). As shown in Fig. 12, the accumulated post-seismic deformation in the coseismic deformation area is ∼0.5 cm in a ∼3-yr period after the main shock. It is reasonable to conclude that the earthquake does not cause notable post-seismic surface deformation.

6 CONCLUSIONS

The 2017 M_w 6.3 Jinghe earthquake occurred in the North Tianshan orogenic zone, which did not rupture to surface, but caused centimeter-level coseismic deformation. We utilize the GACOS model to remove the atmospheric delay in the InSAR deformation maps. The ascending and descending coseismic deformation fields are extracted and then used to invert for the earthquake source geometric parameters and slip distribution. The focal mechanism, the seismogenic faulting geometry, and the aftershock distribution are discussed. The main conclusions are drawn as follows.

(1) Accurate coseismic deformation is derived from the multiple InSAR processing after GACOS atmospheric corrections. The signal-to-noise of the coseismic deformation maps is improved. Results show that the coseismic deformation field is located to the west of the mian shock with a maximum displacement of ∼6 cm. The coseismic deformation pattern implies that the Jinghe earthquake is a thrust and unilateral rupture event.

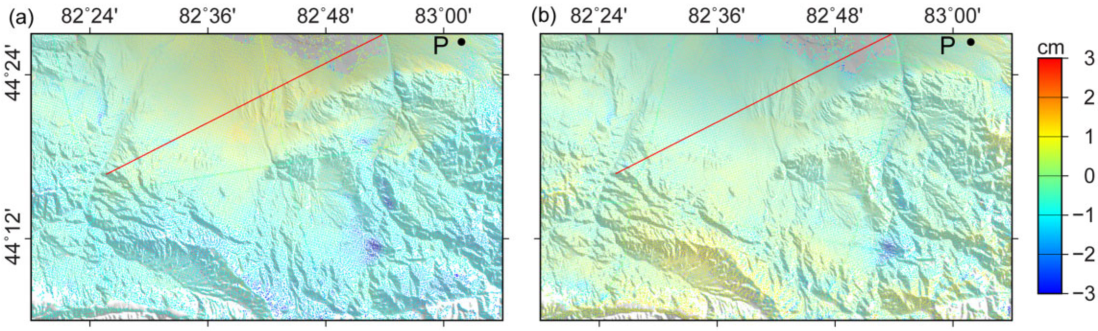

Figure 12. Maps of accumulated post-seismic deformation. (a) Ascending orbit. (b) Descending orbit.

(2) A new blind fault with a strike of 62° and a south-dipping angle of ∼28° is identified to be the causative fault of the 2017 Jinghe earthquake. The newly identified blind fault was developed beneath the Yongji fold, refuting that the earthquake was ascribed to the rupture of the pre-existing Kusongmuqike piedmont fault or a pure east–west striking fault assumed by previous research. Our fault model shows that the aftershock distribution generally agrees with the slip distribution.

(3) No significant post-seismic deformation is observed over ∼3-yr period following the main shock.

ACKNOWLEDGMENTS

This work was supported by the National Natural Science Foundation of China under Grant Nos. 41874024 and 41611530702, the National Key R&D Program of China under Grant No. 2017YFB0502700 and the Special Fund of the Institute of Earthquake Forecasting, China Earthquake Administration under Grant No. 2019IEF0702. Jianming Liu from Earthquake Administration of Xinjiang Uygur Autonomous Region is thanked for providing the relocated aftershock catalogue.

DATA AVAILABILITY

Sentinel-1A SAR data were acquired from the ESA website (https://scihub.copernicus.eu/dhus/#/home, last accessed February 2018). The POD precise orbit ephemerides were downloaded from the Sentinel-1 POD service website (https://qc.sentinel1.eo.esa.int/aux_poeorb/, last accessed February 2018). The SRTM DEM data were downloaded from NASA's Land Processes Distributed Active Archive Center (LP DAAC), located at the USGS Earth Resources Observation and Science (EROS) Center (https://e4ftl01.cr.usgs.gov/SRTM/SRTMGL1.003/2000.02.11/, last accessed November 2017). GACOS tropospheric delay maps were downloaded from the Generic Atmospheric Correction Online Service website (http://www.gacos.net/, last accessed March 2018). The GCMT database was from the website (http://www.globalcmt.org/CMTsearch.html, last accessed August 2017). The USGS database was from the website (https://earthquake.usgs.gov/earthquakes/search/, last accessed August 2017). The CENC earthquake database was from their website (http://www.ceic.ac.cn/history, last accessed August 2017). The fault data was downloaded from the SAFSDC (http://activefault-datacenter.cn/, last accessed October 2017). Some plots were generated using the Generic Mapping Tools version 5.3.3 (http://www.soest.hawaii.edu/gmt, last accessed October 2017).

REFERENCES

Bagnardi, M. & Hooper, A., 2018. Inversion of surface deformation data for rapid estimates of source parameters and uncertainties: a Bayesian approach, *Geochem. Geophys. Geosyst.,* **19,** 2194–2211.

Berardino, P., Fornaro, G., Lanari, R. & Sansosti, E., 2002. A new algorithm for surface deformation monitoring based on small baseline differential SAR interferograms, *IEEE Trans. Geosci. Remote Sens.,* **40,** 2375–2383.

Chen, C.W. & Zebker, H.A., 2001. Two-dimensional phase unwrapping with use of statistical models for cost functions in nonlinear optimization, *J. Opt. Soc. Am. A,* **18,** 338–351.

Chen, J., Shen, J., Li, J., Yang, J., Hu, W., Zhao, X. & Zeng, X., 2007. Preliminary study on new active characteristics of Kusongmuxieke Mountain front fault in the western segment of North Tianshan, *Northwestern Seismol. J.,* **29**(4), 335–340(in Chinese).

Chen, J., Tan, M., Wu, G., Hu, W., Sun, J. & Zhang, Z., 2012. The characteristic of seismic hazard and seismogenic structure of Jinghe earthquake with Ms5.0 Xinjiang on Oct 16th, 2011, *Inland Earthq.,* **26**(3), 233–241(in Cinese).

Ding, X., Li, Z., Zhu, J., Feng, G. & Long, J., 2008. Atmospheric effects on InSAR measurements and their mitigation, *Sensors,* **8,** 5426–5448.

Fattahi, H., Amelung, F., Chaussard, E. & Wdowinski, S., 2015. Coseismic and postseismic deformation due to the 2007 M5.5 Ghazaband fault earthquake, Balochistan, Pakistan, *Geophys. Res. Lett.,* **42,** 3305–3312.

Feng, J., Zhen, W. & Wu, Z., 2017. Ionospheric effects on repeat-pass SAR interferometry, *Adv. Space Res.,* **60**(7), 1504–1515.

Feng, W., Samsonov, S., Li, P. & Omari, K., 2016. Coseismic and early-postseismic displacements of the 2015 M_w8.3 Illapel (Chile) earthquake imaged by Sentinel-1a and RADARSAT-2, in *Proceedings of the IEEE 2016 International Geoscience and Remote Sensing Symposium (IGARSS),* Beijing, China, pp. 5990–5993.

Feng, W.P. & Li, Z.H.. 2010. A novel hybrid PSO /simplex algorithm for determining earthquake source parameters using InSAR data, *Prog. Geophys.,* **25,** 1189–1196(in Chinese).

Ferretti, A., Prati, C. & Rocca, F., 2001. Permanent scatterers in SAR interferometry, *IEEE Trans. Geosci. Remote Sens.,* **39,** 8–20.

Goldstein, R.M. & Werner, C.L., 1998. Radar interferogram filtering for geophysical applications, *Geophys. Res. Lett.,* **25**(21), 4035–4038.

Gong, W., Zhang, Y., Li, T., Wen, S., Zhao, D., Hou, L. & Shan, X., 2019. Multi-sensor geodetic observations and modeling of the 2017 M_w 6.3 Jinghe earthquake, *Remote Sens.*, **11,** 2157.

Jiang, H., Feng, G., Wang, T. & Bürgmann, R., 2016. Toward full exploitation of coherent and incoherent information in Sentinel-1 TOPS data for retrieving surface displacement: application to the 2016 Kumamoto (Japan) earthquake, *Geophys. Res. Lett.,* 10.1002/2016GL072253.

Jung, H.S. & Lee, W.J., 2015. An improvement of ionospheric phase correction by multiple-aperture interferometry (MAI), *IEEE Trans. Geosci. Remote Sens.,* **53,** 4952–4960.

Jung, H.S., Lee, D.T., Lu, Z. & Won, J.S., 2013. Ionospheric correction of SAR interferograms by multiple-aperture interferometry, *IEEE Trans. Geosci. Remote Sens.,* **51,** 3191–3199.

Hooper, A. & Zebker, H. A., 2007. Phase unwrapping in three dimensions with application to InSAR time series, *J. Opt. Soc. Am. A,* **24**(9), 2737–2747.

Hooper, A., Bekaert, D., Spaans, K. & Arikan, M., 2012. Recent advances in SAR interferometry time series analysis for measuring crustal deformation, *Tectonophysics,* **514–517,** 1–13. doi:10.1016/j.tecto.2011.10.013.

Laske, G., Masters, G., Ma, Z. & Pasyanos, M., 2013. Update on CRUST1.0—a 1-degree Global Model of Earth's Crust, *Geophys. Res. Abstracts,* **15,** Abstract EGU2013-2658.

Lee, W.J., Lu, Z., Jung, H.S. & Ji, L., 2017. Measurement of small co-seismic deformation field from multitemporal SAR interferometry: application to the 19 September 2004 Huntoon Valley earthquake, *Geomatics Nat. Hazards Risk,* **8**(2), 1241–1257.

Li, Y. & Wang, C., 2019. Focal mechanism solution and stress field characteristics in source area of Jinghe M_s 6.6 earthquake sequence on August 9, 2017, *China Earthq. Eng. J.,* **41**(5), 1820–1289(in Chinese).

Li, Z., 2005. Correction of atmospheric water vapor effects on repeat-pass SAR interferometry using GPS, MODIS and MERIS data, *PhD dissertation*, University of London.

Li, Z., Muller, J., Cross, P. & Fielding, E.J., 2005. Interferometric synthetic aperture radar (InSAR) atmospheric correction: GPS, moderate resolution imaging spectroradiometer (MODIS), and InSAR integration, *J. geophys. Res.,* **110**. doi:10.1029/2004JB003446.

Liu, C., Qiu, J. & Wang, J., 2018. The 2017 Jinghe M_s 6.6 earthquake inversion from ascending and descending Sentinel-1 observations, *J. Geod. Geodyn.,* **38**(11), 1111–1116(in Chinese).

Liu, J., Gao, R., Wang, Q. & Nie, X., 2017. Relocation of the Jinghe M_s 6.6 earthquake sequence on August 9, 2017 and analysis of the seismogenic structure, *Earthq. Res. China,* **33**(4), 663–670(in Chinese).

Liu, Z., Jung, H.S. & Lu, Z., 2014. Joint correction of ionosphere noise and orbital error in L-band SAR interferometry of interseismic deformation in southern California, *IEEE Trans. Geosci. Rem. Sens.,* **52,** 3421–3427.

Liu, Z., Wan, Y., Huang, J., Jin, Z., Yang, F. & Li, Y., 2019. The tectonic stress field adjacent to the source of the 2017 Jinghe M_s 6.6 earthquake and slip property of its seismogenic fault, *Chin. J. Geophys.,* **62**(4), 1336–1348(in Chinese).

Lu, Z. & Dzurisin, D., 2014. *InSAR Imaging of Aleutian Volcanoes: Monitoring a Volcanic Arc from Space,* Springer Nature.

Meyer, F.J., Bamler, R., Jakowski, N. & Fritz, T., 2006. The potential of low-frequency SAR systems for mapping ionospheric TEC distributions, *IEEE Geosci. Remote Sens. Lett.,* **3**(4), 560–564.

Okada, Y., 1985. Surface deformation due to shear and tensile faults in a half-space. *Bull. seism. Soc. Am.,* **75**(4), 1135–1154.

Rosen, P.A., Gurrola, E., Sacco, G.F. & Zebker, H., 2012. The InSAR scientific computing environment, in *European Conference on Synthetic Aperture Radar,* VDE, pp. 730–733.

Sieh, K.E., 1978. Slip along San-Andreas fault associated with great 1857 earthquake, *Bull. seism. Soc. Am.,* **68**(5), 1421.

Sun, J. & Zhang, Z., 2009. Syntectonic growth strata and implications for late Cenozoic tectonic uplift in the northern Tian Shan, China, *Tectonophysics,* **463,** 60–68.

Sun, J., Shen, Z., Li, T. & Chen, J., 2016. Thrust faulting and 3D ground deformation of the 3 July 2015 M_w 6.4 Pishan, China earthquake from Sentinel-1A radar interferometry, *Tectonophysics,* **683,** 77–85.

Wang, R., Diao, F. & Hoechner, A., 2013. SDM—a geodetic inversion code incorporating with layered crust structure and curved fault geometry, in *EGU General Assembly,* Vienna, Austria, EGU2013–2411.

Wen, Y., Xu, C., Liu, Y. & Jiang, G., 2016. Deformation and source parameters of the 2015 M_w 6.5 earthquake in Pishan, western China, from Sentinel-1A and ALOS-2 data, *Remote Sens.,* **8,** 134.

Werner, M., 2001. Shuttle Radar Topography Mission (SRTM) mission overview, *J. Telecommun.,* **55**(3–4), 75–79.

Xu, Z., Liang, S., Liu, J., Zou, L. & Liu, J., 2019. Focal mechanism solution and relocation of the aftershock sequences of the 2017 Jinghe M_s 6.6 earthquake in Xinjiang, *Prog. Geophys.,* **34**(4), 1357–1365(in Chinese).

Yu, C., Penna, N.T. & Li, Z., 2017. Generation of real-time mode high resolution water vapor fields from GPS observations, *J. geophys. Res.,* **122,** 2008–2025.

Yu, C., Li, Z., Chen, J. & Hu, J.C., 2018. Small magnitude co-seismic deformation of the 2017 Mw 6.4 Nyingchi earthquake revealed by InSAR measurements with atmospheric correction, *Remote Sens.*, **10,** 684.

Yu, C., Li, Z. & Penna, N.T., 2020. Triggered afterslip on the southern Hikurangi subduction interface following the 2016 Kaikōura earthquake from InSAR time series with atmospheric corrections, *Remote Sens. Environ.,* **251,** 112097.

Zebker, H.A., Rosen, A. & Hensley, S., 1997. Atmospheric effects in interferometric synthetic aperture radar surface deformation and topographic maps, *J. geophys. Res.,* **102,** 7547–7563.

Zhang, X. *et al.*, 2020. Source characteristics of the 2017 M_s 6.6 (M_w 6.3) Jinghe earthquake in the northeastern Tien Shan, *Seismol. Res. Lett.,* **91,** 745–757.

Zubovich, A.V. *et al.*, 2010. GPS velocity field for the Tien Shan and surrounding regions, *Tectonics,* **29**(6), TC6014, doi:10.1029/2010TC002772.

SUPPORTING INFORMATION

Supplementary data are available at *GJI* online.

Figure S1. Marginal posterior probability distributions from GBIS inversion for the north-dipping fault model parameters. (a and b) Upper bounds of the dip slip are set to 0.4 and 0.6 m, respectively. Red lines represent the maximum a posterior probability solution. Scatter plots are contoured according to frequency.

Figure S2. Coseismic slip distribution with (a) homogeneous crust model and (b) layered crust model. We resolved the coseismic slip distribution with a homogeneous crust model and compare it with the layered crust model using SDM (Wang *et al.* 2013). There are no visible discrepancies on the slip distribution derived by the different crust model for this case.

Figure S3. Checkerboard resolution test for the inversion of coseismic slip distribution, with each patch size of 3 km × 3 km. (a) 3 × 3 checkerboard input model; (b) recovered resolution of 3 × 3 patches constrained by the InSAR data. The figure shows the checkerboard test for the inversion of coseismic slip distribution. Most of the slip patches with a depth (along dip direction) smaller than 25 km are recovered in the checkerboard test.

Figure S4. Post-seismic deformation time-series of ascending orbit T85. Negative values denote motion away from the satellite in the LOS direction and positive values denote motion towards the satellite. We use StaMPS method (Hooper *et al.* 2012) to derive post-seismic deformation.

Figure S5. Post-seismic deformation time-series of descending orbit T63. Negative values denote motion away from the satellite in LOS direction and positive values denote motion towards the satellite. We use StaMPS method (Hooper *et al.* 2012) to derive post-seismic deformation.

Table S1. Sentinel-1A SAR data used for deriving coseismic deformation.

Table S2. Layered elastic earth model.

Table S3. Multitemporal Sentinel-1 SAR data for post-seismic deformation.